

# DRAFT

# CMS Paper

*The content of this note is intended for CMS internal use and distribution only*

2025/04/15

Archive Hash: 32611a6

Archive Date: 2023/09/28

## Search for dark matter produced in association with a resonant bottom quark pair in proton-proton collisions at $\sqrt{s} = 13 \text{ TeV}$

The CMS Collaboration

### Abstract

A search for dark matter produced in association with a resonant bottom quark pair has been performed in proton-proton collisions at a center-of-mass energy of 13 TeV collected with the CMS detector during the 2016–2018 data taking period at the CERN LHC. The analyzed data sample corresponds to an integrated luminosity of  $138 \text{ fb}^{-1}$ . The results are interpreted in terms of a novel theoretical model of dark matter production that, together with a spin-1 gauge boson mediator, predicts the existence a Higgs-boson-like particle in the dark sector (i.e., a dark Higgs boson). The model provides simultaneously a mechanism to generate the masses of particles in the dark sector and a new annihilation channel that helps relax the constraints on dark matter relic abundance. If such a dark Higgs boson mixes with the standard model Higgs boson, its decay into a bottom quark pair can be identified in hadronic jets. This search focuses on final states where the dark Higgs boson is produced in association with the dark matter mediator. It gives rise to an experimental signature with a large missing transverse momentum. Limits at 95% confidence level on the signal strength for dark Higgs boson mass hypotheses below 160 GeV are set for the first time with CMS data. Values of the mediator mass up to 2.5–4.5 TeV are excluded depending on the dark Higgs boson mass.

This box is only visible in draft mode. Please make sure the values below make sense.

PDFAuthor:	M. Cremonesi, A. Das, M. Donega, S. Eisenberger, E. Ertorer, A. Hall, M. Hildreth, B. Jayatilaka, J. Lee, N. Macilla, M. Marchegiani, C.-S. Moon, I. Pedraza, N. Smith, T. Tomei, D. Valsecchi, R. Wallny, M. Wassmer1, Z. Ye
PDFTitle:	Search for Dark Matter Produced in Association with a Resonant Bottom-Quark Pair
PDFSubject:	CMS
PDFKeywords:	CMS, physics, software, computing

Please also verify that the abstract does not use any user defined symbols



## 1 Introduction

The predictions of the standard model (SM) of particle physics have been confirmed by decades of experiments. Despite these successes, the SM is still not able to explain phenomena such as the existence of dark matter (DM). While astrophysical observations have established that most of the matter in the Universe is composed of DM [1], details of its nature remain elusive.

One theoretically attractive model of DM is that of a thermally produced weakly interacting massive particle (WIMP). The existence of such a particle, with the right mass and couplings, could explain the abundance of DM in the universe, as well as many of the observed phenomena commonly ascribed to DM [2]. If non-gravitational interactions exist between DM and SM particles, then the new interaction would imply the existence of a new mediator, and the Large Hadron Collider (LHC) would have the unique possibility to directly produce it along with the DM particles themselves, and study their properties.

Simplified models of DM production at the LHC [3] have become increasingly popular in recent years. These models predict that the pair production of DM particles in hadron collisions proceeds through a spin-0 or spin-1 bosonic mediator produced in the s-channel. Such a mediator is then accompanied by some other SM visible particle, often emitted as initial-state radiation (ISR). This gives rise to experimental signatures where the mediator decays into weakly interacting DM particles, appearing as an imbalance in the transverse momentum. Such signatures are commonly referred to as “mono-X”, where X denotes either the SM particle produced in association with DM (such as a mono-photon or mono-W/Z) or its detector manifestation (such as a mono-jet).

Among these, mono-jet final states—where a gluon or quark is emitted as initial-state radiation and appears in the detector as a hadronic jet—offer a favorable topology due to the high rate of radiation of quarks and gluons in the initial state. Mono-jet searches at the LHC [4, 5] have strongly constrained the DM parameter space, in models where DM relic particles in the cosmos would annihilate directly into final state SM particles. The tension with astrophysical measurements of the abundance of DM is relaxed if the DM particles are not the lightest dark sector particles, leading to new annihilation channels.

The theoretical framework can therefore be extended by models where, together with a spin-1 gauge boson  $Z'$ , a new complex Higgs field is introduced, whose vacuum expectation value spontaneously breaks the gauge symmetry in the dark sector [6], giving rise to a new physical “dark” Higgs boson  $H_D$ . If the  $H_D$  boson is sufficiently light, DM particles can annihilate into a  $H_D$  boson pair. This new annihilation channel would allow the model to easily match the observed relic abundance [7–9]. In this model, the DM particle  $\chi$  is taken to be a Majorana fermion that couples axially to the gauge boson  $Z'$ . The  $Z'$  boson also has a vector-like coupling with SM quarks. The relevant part of the spin-1 sector of the model Lagrangian is:

$$\mathcal{L}_{\text{spin-1}} \supset -g_\chi Z'_\mu \bar{\chi} \gamma^\mu \gamma^5 \chi - g_q Z'_\mu \sum_q \bar{q} \gamma^\mu q,$$

where  $g_\chi$  is the coupling between  $Z'$  mediator and the  $\chi$  particles, while  $g_q$  is the coupling between the  $Z'$  mediator and the SM quarks. These two parameters are set to 1.0 and 0.25, respectively, in accordance with the LHC Dark Matter Working Group recommendations [10].

As the lightest state in the dark sector, the  $H_D$  boson does not decay into  $\chi$  particles, but it can decay into visible SM particles via mixing with the SM Higgs ( $H$ ) boson [8, 11]. For this reason, the decay into a b-quark pair is expected to be dominant for  $H_D$  bosons with masses below 135 GeV, and is significant for masses up to 160 GeV. The mixing angle  $\theta_h$  between the  $H_D$  boson

44 and the SM H boson is set to 0.01, a value that is large enough to ensure prompt decay of the  
 45  $H_D$  boson while being small enough to have no observable effect on the the SM Higgs boson  
 46 couplings [12].

47 In this paper, we present a search for DM in events where  $\chi$  particles are produced in associa-  
 48 tion with a  $H_D$  boson decaying into a b-quark pair. The production mechanism is shown in  
 49 Fig. 1. A  $Z'$  boson is produced by a quark-antiquark interaction in the initial state. It radiates a  
 50  $H_D$  boson via dark-Higgsstrahlung before decaying into a pair of  $\chi$  particles.

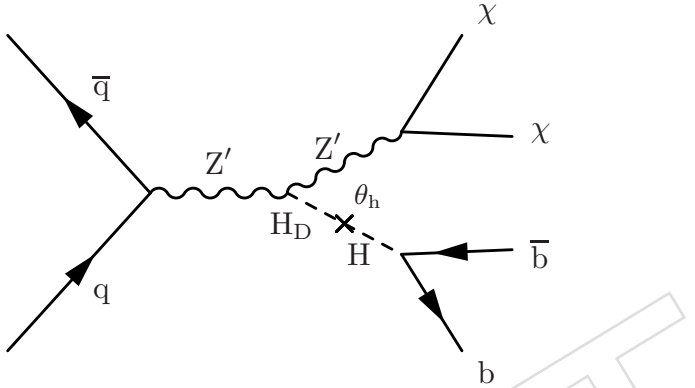


Figure 1: Feynman diagram for the associated production of a  $H_D$  boson and  $\chi$  particles. The interaction with SM quarks is mediated by a  $Z'$  boson, and the  $H_D$  boson mixes with the SM Higgs boson through the  $\theta_h$  mixing angle. In this paper we focus on the decay of the  $H_D$  boson into a b-quark pair, which is dominant at lower masses.

51 Searches for  $H_D$  bosons produced in association with DM have already been performed by  
 52 the ATLAS [13] and CMS [14] collaborations. These searches focus on heavier  $H_D$  boson mass  
 53 hypotheses, larger than 160 GeV. For a  $H_D$  boson of such a mass the decay into a pair of W  
 54 bosons is dominant. The ATLAS collaboration has also recently published a search for lower  
 55 mass  $H_D$  bosons decaying into a b-quark pair [15]. In this paper, we describe a similar search  
 56 which uses the full dataset collected by the CMS experiment at a center-of-mass energy of 13  
 57 TeV during the 2016–2018 data taking period, corresponding to an integrated luminosity of  
 58  $138 \text{ fb}^{-1}$ .

## 59 2 The CMS detector and event reconstruction

60 The CMS apparatus [16, 17] is a multipurpose, nearly hermetic detector, designed to trigger  
 61 on [18–20] and identify electrons, muons, photons, and (charged and neutral) hadrons [21–23].  
 62 Its central feature is a superconducting solenoid of 6 m internal diameter, providing a mag-  
 63 netic field of 3.8 T. Within the solenoid volume are a silicon pixel and strip tracker, a lead  
 64 tungstate crystal electromagnetic calorimeter (ECAL), and a brass and scintillator hadron cal-  
 65 orimeter (HCAL), each composed of a barrel and two endcap sections. Forward calorimeters  
 66 extend the pseudorapidity coverage provided by the barrel and endcap detectors. Muons are  
 67 reconstructed using gas-ionization detectors embedded in the steel flux-return yoke outside  
 68 the solenoid. More detailed descriptions of the CMS detector, together with a definition of the  
 69 coordinate system used and the relevant kinematic variables, can be found in Refs. [16, 17].

70 The silicon tracker used in 2016 measured charged particles within the range  $|\eta| < 2.5$ . For  
 71 nonisolated particles of  $1 < p_T < 10 \text{ GeV}$  and  $|\eta| < 1.4$ , the track resolutions were typically  
 72 1.5% in  $p_T$  and 25–90 (45–150)  $\mu\text{m}$  in the transverse (longitudinal) impact parameter [23]. At the  
 73 start of 2017, a new pixel detector was installed [24]; the upgraded tracker measured particles

<sup>74</sup> up to  $|\eta| = 3.0$  with typical resolutions of 1.5% in  $p_T$  and  $20\text{--}75 \mu\text{m}$  in the transverse impact  
<sup>75</sup> parameter [25] for nonisolated particles of  $1 < p_T < 10 \text{ GeV}$ . According to simulation studies  
<sup>76</sup> [26], similar improvements are expected in the longitudinal direction. The primary vertex  
<sup>77</sup> (PV) is taken to be the vertex corresponding to the hardest scattering in the event, evaluated  
<sup>78</sup> using tracking information alone, as described in Section 9.4.1 of Ref. [27].

<sup>79</sup> In the region  $|\eta| < 1.74$ , the HCAL cells have widths of 0.087 in pseudorapidity and 0.087  
<sup>80</sup> in azimuth ( $\phi$ ). In the  $\eta\text{-}\phi$  plane, and for  $|\eta| < 1.48$ , the HCAL cells map on to  $5\times 5$  arrays  
<sup>81</sup> of ECAL crystals to form calorimeter towers projecting radially outwards from close to the  
<sup>82</sup> nominal interaction point. For  $|\eta| > 1.74$ , the coverage of the towers increases progressively  
<sup>83</sup> to a maximum of 0.174 in  $\Delta\eta$  and  $\Delta\phi$ . The forward hadron (HF) calorimeter uses steel as an  
<sup>84</sup> absorber and quartz fibers as the sensitive material. The two halves of the HF are located 11.2 m  
<sup>85</sup> from the interaction region, one on each end, and together they provide coverage in the range  
<sup>86</sup>  $3.0 < |\eta| < 5.2$ . They also serve as luminosity monitors.

<sup>87</sup> Events of interest are selected using a two-tiered trigger system. The first level (L1), composed  
<sup>88</sup> of custom hardware processors, uses information from the calorimeters and muon detectors to  
<sup>89</sup> select events at a rate of around 100 kHz within a fixed latency of  $4 \mu\text{s}$  [18]. The second level,  
<sup>90</sup> known as the high-level trigger (HLT), consists of a farm of processors running a version of the  
<sup>91</sup> full event reconstruction software optimized for fast processing, and reduces the event rate to  
<sup>92</sup> a few kHz before data storage [19, 20].

<sup>93</sup> A particle-flow (PF) algorithm [28] aims to reconstruct and identify each individual particle in  
<sup>94</sup> an event, with an optimized combination of information from the various elements of the CMS  
<sup>95</sup> detector. In this process, the identification of the PF candidate type (photon, electron, muon,  
<sup>96</sup> and charged and neutral hadrons) plays an important role in the determination of the particle  
<sup>97</sup> direction and energy. The energy of photons is obtained from the ECAL measurement. The  
<sup>98</sup> energy of electrons is determined from a combination of the electron momentum at the primary  
<sup>99</sup> interaction vertex as determined by the tracker, the energy of the corresponding ECAL cluster,  
<sup>100</sup> and the energy sum of all bremsstrahlung photons spatially compatible with originating from  
<sup>101</sup> the electron track. The energy of muons is obtained from the curvature of the corresponding  
<sup>102</sup> track. The energy of charged hadrons is determined from a combination of their momentum  
<sup>103</sup> measured in the tracker and the matching ECAL and HCAL energy deposits, corrected for  
<sup>104</sup> the response function of the calorimeters to hadronic showers. Finally, the energy of neutral  
<sup>105</sup> hadrons is obtained from the corresponding corrected ECAL and HCAL energies.

<sup>106</sup> In this search, electrons (photons) are required to have  $p_T > 10$  (15) GeV and  $|\eta| < 2.5$ . Muons  
<sup>107</sup> are required to have  $p_T > 10 \text{ GeV}$  and  $|\eta| < 2.4$ . All leptons and photons are required to be  
<sup>108</sup> isolated. Isolation is calculated imposing thresholds on the energy of PF candidates within a  
<sup>109</sup> certain distance  $\Delta R = \sqrt{(\Delta\phi^2 + \Delta\eta^2)}$  with respect to the lepton/photon. Additional selection  
<sup>110</sup> criteria are applied to define “loose” (“veto”) electrons (muons and photons) [21, 22], which  
<sup>111</sup> are used to reject unwanted events. Similarly, “tight” leptons/photons are defined and used to  
<sup>112</sup> select events in control data samples.

<sup>113</sup> Hadronically decaying tau leptons are required to pass identification criteria using the hadron-  
<sup>114</sup> plus-strips algorithm [29]. In addition, a new algorithm for the identification of hadronic tau  
<sup>115</sup> lepton decays, called DEEPTAU [30], is used. The DEEPTAU algorithm is based on multi-  
<sup>116</sup> classification and provides classifiers to discriminate genuine hadronic tau lepton decays from  
<sup>117</sup> jets, electrons, and muons. Nonetheless, the overlap with electrons and muons is accounted for  
<sup>118</sup> by removing tau leptons that are within a distance  $\Delta R < 0.4$  around a well reconstructed and  
<sup>119</sup> isolated electron or muon.

For each event, hadronic jets are clustered from the PF candidates using the infrared and collinear safe anti- $k_T$  algorithm [31, 32] with a distance parameter of 0.4 or 1.5. Depending on the respective distance parameter, these jets are referred to as “AK4” or “AK15” jets. Jet momentum is determined as the vectorial sum of all particle momenta in the jet, and is found from simulation to be, on average, within 5 to 10% of the true momentum over the whole  $p_T$  spectrum and detector acceptance. Jet energy corrections are derived from simulation to bring the measured response of jets to that of particle level jets on average. In situ measurements of the momentum balance in dijet, photon + jet, Z + jet, and multijet events are used to account for any residual differences in the jet energy scale between data and simulation [33]. The jet energy resolution amounts typically to 15–20% at 30 GeV, 10% at 100 GeV, and 5% at 1 TeV [33]. Additional selection criteria are applied to each jet to remove jets potentially dominated by anomalous contributions from various subdetector components or reconstruction failures.

Additional proton-proton interactions within the same or nearby bunch crossings (pileup) can contribute additional tracks and calorimetric energy depositions to the jet momentum. To mitigate this effect in the AK4 jets, charged particles identified to be originating from pileup vertices are discarded and an offset correction is applied to correct for remaining contributions. For the AK15 jets, the pileup per particle identification algorithm (PUPPI) [34, 35] is used to mitigate the effect of pileup at the reconstructed particle level, making use of local shape information, event pileup properties, and tracking information. A local shape variable is defined, which distinguishes between collinear and soft diffuse distributions of other particles surrounding the particle under consideration. The former is attributed to particles originating from the hard scatter and the latter to particles originating from pileup interactions. Charged particles identified to be originating from pileup vertices are discarded. For each neutral particle, a local shape variable is computed using the surrounding charged particles compatible with the primary vertex within the tracker acceptance ( $|\eta| < 2.5$ ), and using both charged and neutral particles in the region outside of the tracker coverage. The momenta of the neutral particles are then rescaled according to their probability to originate from the primary interaction vertex deduced from the local shape variable, superseding the need for jet-based pileup corrections [34].

The AK4 jets used in this search are further required to have a  $p_T$  larger than 30 GeV and  $|\eta| < 2.5$ . Jets with  $\Delta R < 0.4$  with respect to a well identified and isolated lepton or photon are removed. To identify jets originated by the hadronization of b quarks (hereafter referred to as “b jets”), the DEEPJET algorithm [36] is employed. A loose working point is used, defined for each year of data-taking as the minimum requirement in the DEEPJET discriminator distribution which returns a 10% rate of misidentifying a jet originated by a light-flavor quark. The loose working point correspond to an efficiency of correctly identifying jets originated by b quarks (i.e. b-tagging efficiency) of 90–95%, depending on the  $p_T$  of the AK4 jet.

The AK15 jets used in this search are further required to have a  $p_T$  larger than 160 GeV and  $|\eta| < 2.4$ . Jets with  $\Delta R < 1.5$  with respect to a well identified and isolated lepton or photon are removed. The modified mass drop tagger algorithm [37, 38], also known as the soft-drop (SD) algorithm, with the angular exponent  $\beta = 0$ , soft cutoff threshold  $z_{\text{cut}} < 0.1$ , and characteristic radius  $R_0 = 1.5$  [39], is applied to remove soft, wide-angle radiation from the jet. To identify AK15 jets that are consistent with the hadronization of a  $b\bar{b}$  pair from the decay of a boosted massive resonance, the DEEPAK15 algorithm [40] is used. More specifically, the “mass-decorrelated” (MD) version of DEEPAK15 is employed. In this variant, an adversarial training is performed in which a second neural network is made to extract the AK15 jet mass from the output of the DEEPAK15 graph neural network. A good performance of this second network yields to a penalty on the joint cost function of the two networks. Therefore, this method optimizes the ability to correctly identify the origin of a AK15 jet while systematically

168 decorrelating the output score from the AK15 jet mass. This approach avoids shaping the AK15  
 169 jet mass distribution in background events. Since the strategy for this search relies on the AK15  
 170 jet mass shape for background estimation, the MD version of the tagger offers the best option.  
 171 Identification working points are defined for each year of data-taking and optimized for this  
 172 specific search.

173 The missing transverse momentum vector  $\vec{p}_T^{\text{miss}}$  is computed as the negative vector sum of  
 174 the transverse momenta of all the PF candidates in an event, and its magnitude is denoted as  
 175  $p_T^{\text{miss}}$ . The  $\vec{p}_T^{\text{miss}}$  is modified to account for corrections to the energy scale and resolution of the  
 176 reconstructed AK4 jets in the event [41]. Anomalous high- $p_T^{\text{miss}}$  events can be due to a variety  
 177 of reconstruction failures, detector malfunctions, or noncollision backgrounds. Such events are  
 178 rejected by dedicated filters that are designed to eliminate more than 85–90% of the spurious  
 179 high- $p_T^{\text{miss}}$  events with a signal efficiency exceeding 99.9% [41]. Since signal events in this search  
 180 contain only jets and no other reconstructed candidates,  $p_T^{\text{miss}}$  is equivalent to the transverse  
 181 momentum of the hadronic recoil, called U. For the leading background processes, this also  
 182 corresponds to the transverse momentum of a vector boson. In the control data samples of  
 183 this search where a lepton in the final state is required,  $p_T^{\text{miss}}$  is not equivalent to U anymore.  
 184 At the same time, U still represents the transverse momentum of the vector boson from those  
 185 background process that populate these samples. Since this search relies on prediction derived  
 186 from data in control samples to constrain the main backgrounds, the U derived in the control  
 187 samples can be used to model the transverse momentum of the vector boson. In the control  
 188 data samples, the variable is computed subtracting from  $\vec{p}_T^{\text{miss}}$  the  $\vec{p}_T$  of the lepton.

### 189 **3 Simulated samples**

190 Samples of Monte Carlo (MC) simulated events are used to predict the signal and background  
 191 contributions. In all cases, parton showering, hadronization, and underlying event properties  
 192 are modeled using PYTHIA [42] version 8.202 or later with the underlying event tune  
 193 CUETP8M1 or CP5 [43], based on the year of data taking. Simulation of interactions between  
 194 particles and the CMS detector is based on GEANT4 [44]. The NNPDF 3.0 next-to-next-to-  
 195 leading order (NNLO) [45] and the NNPDF 3.1 NNLO [46] parton distribution functions (PDFs)  
 196 are used for the generation of all samples based on the year of data taking. The same recon-  
 197 struction algorithms used for the data are applied to simulated samples.

198 For the associated production of SM vector bosons and jets (V + jets production), predictions  
 199 with up to two partons in the final state are obtained at leading order (LO) in QCD using  
 200 MADGRAPH5\_aMC@NLO [47] with the MLM matching scheme [48] between the jets from the  
 201 matrix element calculations and the parton shower. Samples of events with top quark pairs ( $t\bar{t}$   
 202 production) are generated at next-to-leading (NLO) in QCD with up to two additional partons  
 203 in the matrix element calculations using MADGRAPH5\_aMC@NLO and the FxFx jet matching  
 204 scheme [49]. Their cross sections are normalized to the inclusive cross section of  $t\bar{t}$  production  
 205 at NNLO in QCD [50]. Events with electroweakly produced single top quarks (single t pro-  
 206 duction) are simulated using POWHEG 2.0 [51, 52] and normalized to the inclusive cross section  
 207 calculated at NLO in QCD [53, 54]. The associated production of vector bosons (VV produc-  
 208 tion) is simulated at NLO in QCD using PYTHIA, and normalized to the cross sections at NNLO  
 209 precision for WW production [55], and at NLO precision for WZ and ZZ production [56]. Sev-  
 210 eral production mechanisms of SM H bosons decaying into a b-quark pair ( $H \rightarrow b\bar{b}$  production)  
 211 are also produced at LO with the POWHEG generator. Samples of QCD multijet production  
 212 events are generated at LO using MADGRAPH5\_aMC@NLO.

213 Simulated samples of  $H_D$  boson production are generated with MADGRAPH5\_aMC@NLO [47]

214 at LO, including up to one additional parton in the matrix element calculations, with the MLM  
 215 matching scheme. Separate samples are generated for different mass hypotheses for the  $Z'$   
 216 mediator,  $\chi$  particles, and  $H_D$  bosons.

## 217 4 Event selection

218 The signal targeted in this analysis displays a large  $p_T^{\text{miss}}$  and an AK15 jet that is identified as  
 219 originating from a  $H_D \rightarrow b\bar{b}$  decay. Events with these characteristics comprise the signal region  
 220 (SR). The leading SM background contributions originate from  $Z(\nu\nu) + \text{jets}$  (hereafter referred  
 221 to as  $Z + \text{jets}$ ), and  $W(e\nu)/W(\mu\nu) + \text{jets}$  production (collectively referred to as  $W + \text{jets}$ ), the  
 222 properties of which are constrained using control regions (CRs) with zero or one charged lep-  
 223 ton, that are enriched in  $Z + \text{jets}$  and  $W + \text{jets}$  events, respectively. Additionally, CRs enriched  
 224 in  $t\bar{t}$  events are also defined. The  $V + \text{jets}$  and  $t\bar{t}$  events in these CRs share many kinematic  
 225 properties of the processes in the SRs and are used to constrain the latter. The CR and SR def-  
 226 definitions share as many of the SR selection criteria as possible, in order to ensure that minimal  
 227 selection biases are introduced. Seven CRs are defined: six single-electron and single-muon  
 228 CRs enriched in  $W + \text{jets}$  and  $t\bar{t}$  events, and a seventh CR enriched in  $Z + \text{jets}$  events. Ad-  
 229 ditional contributions from minor background processes such as  $H \rightarrow b\bar{b}$ ,  $Z(\ell\ell) + \text{jets}$  (hereafter  
 230 referred to as DY+jets), QCD multijet, VV, and single t production are modelled using MC  
 231 simulation.

232 Events in the SR are collected by trigger selections based on two variables. The first is  $p_T^{\text{miss}}$ ,  
 233 which is calculated using all PF candidates reconstructed at the HLT except for muons. The  
 234 second variable, called  $H_T^{\text{miss}}$ , is defined as the magnitude of the negative vector sum of  $\vec{p}_T$  of  
 235 the hadronic jets in the event, using the AK4 jets clustered by the HLT reconstruction. The  
 236 trigger selects events with both  $p_T^{\text{miss}} > 120 \text{ GeV}$  and  $H_T^{\text{miss}} > 120 \text{ GeV}$ . At the HLT, events with high-  
 237  $p_T$  muons are therefore also assigned large  $p_T^{\text{miss}}$ , and the same trigger is used to collect data  
 238 populating the single-muon CRs.

239 The control samples with electrons are selected using two single-electron triggers: one that  
 240 requires  $p_T > 27$  (2016), 35 (2017), 32 (2018) GeV, while the other requires  $p_T > 105$  (2016),  
 241 115 (2017–2018) GeV. Additionally, a single-photon trigger with  $p_T > 200$  GeV is used in 2017  
 242 and 2018. The single-electron triggers differ in their isolation requirements: while the lower  
 243 threshold trigger requires electrons to be well isolated, the higher-threshold trigger does not,  
 244 which improves the efficiency at high  $p_T$ . Similarly, the single-photon trigger avoids reliance  
 245 on the HLT track reconstruction and increases the overall efficiency for electrons with  $p_T >$   
 246 200 GeV. During the 2016 and 2017 data taking, a gradual shift in the timing of the inputs of  
 247 the ECAL L1 trigger in the region  $|\eta| > 2.0$  caused a specific trigger inefficiency, known as L1  
 248 pre-firing. Correction factors are computed from data and applied to the acceptance evaluated  
 249 by simulation for the 2016 and 2017 samples.

250 Events in SR are selected with a requirement of  $p_T^{\text{miss}} > 250$  GeV. The soft-drop corrected mass  
 251 ( $m_{\text{SD}}$ ) of the leading AK15 jet in  $p_T$  must satisfy the requirement  $m_{\text{SD}} \in [40, 300]$ . In order to  
 252 preferentially select events where the leading AK15 jet originates from the hadronic decay of a  
 253  $H_D$  boson, the jet is further required to satisfy a minimum requirement in the DEEPAK15 score.  
 254 A different threshold is used for each year of data-taking, optimized against signal sensitivity.

255 The main background processes in this search are from  $Z + \text{jets}$ ,  $W + \text{jets}$ , and  $t\bar{t}$  produc-  
 256 tion. The  $Z + \text{jets}$  process is the largest background and is irreducible. In contrast, the back-  
 257 ground from  $W + \text{jets}$  and  $t\bar{t}$  processes are suppressed by rejecting events if they contain a  
 258 well-reconstructed and isolated lepton. For electrons, the veto working point is used in their

identification, while the loose working point is used in the identification of muons. Events that contain a loose photon are also rejected. This helps to suppress electroweak backgrounds in which a photon is radiated from the initial state. The  $t\bar{t}$  process is further suppressed by vetoing events with b-tagged AK4 jets that do not overlap with the leading AK15 jet. Finally, to reject QCD multijet events with large  $p_T^{\text{miss}}$  arising from mismeasurements of the jet momenta, a minimum requirement is imposed on the azimuthal separation between the  $\vec{p}_T^{\text{miss}}$  direction and each AK4 jet in the event to be larger than 0.5 radians. Similarly, the azimuthal angle between the  $\vec{p}_T^{\text{miss}}$  direction and each AK15 jet in the event must be larger than 1.5 radians.

To avoid events with anomalous  $p_T^{\text{miss}}$  due to reconstruction failures of the PF algorithm, events are required to have  $|p_T^{\text{miss}}(\text{PF}) / p_T^{\text{miss}}(\text{calorimeter}) - 1| < 0.5$ , where  $p_T^{\text{miss}}(\text{calorimeter})$  is the missing transverse momentum calculated using the information from calorimeter towers. To mitigate mismeasurement from a nonfunctioning HCAL section in 2018 data, events with jets in that region or with  $\phi(\vec{p}_T^{\text{miss}}) \in [-1.62, -0.62]$  at low  $p_T^{\text{miss}}$  are rejected.

As shown in Table 1, even after the full SR selection is applied, the selected data sample still has a large contamination from  $Z + \text{jets}$ ,  $W + \text{jets}$ , and  $t\bar{t}$  production. In order to predict and constrain these background processes, dedicated CRs are used.

Table 1: Expected yields from background processes in SR. The values shown are from MC simulation and the uncertainties are statistical-only.

	2016	2017	2018
$H \rightarrow b\bar{b}$	$57.6 \pm 0.3$	$72.0 \pm 0.3$	$83.8 \pm 0.3$
$Z(\rightarrow \ell\ell) + \text{jets}$	$56.8 \pm 2.2$	$43.3 \pm 2.0$	$37.1 \pm 3.0$
QCD multijet	$93.3 \pm 25.8$	$154.9 \pm 41.7$	$163.2 \pm 64.6$
VV	$718.0 \pm 17.5$	$623.4 \pm 17.8$	$606.4 \pm 20.8$
Single t	$646.0 \pm 10.9$	$567.4 \pm 12.5$	$614.6 \pm 12.8$
$t\bar{t}$	$5486.5 \pm 199.7$	$5810.7 \pm 60.0$	$6784.2 \pm 133.7$
$W + \text{jets}$	$3997.8 \pm 38.5$	$2991.0 \pm 40.2$	$2826.6 \pm 50.5$
$Z + \text{jets}$	$7514.8 \pm 29.2$	$7035.2 \pm 33.3$	$6978.5 \pm 38.8$
Total background	$18570.7 \pm 208.1$	$17297.9 \pm 92.4$	$18094.2 \pm 163.4$

A CR enriched in  $Z + \text{jets}$  production events is identified using the same requirements that define the SR, but inverting the criterion on the DEEPAK15 score.

Similarly, CRs enriched in  $W + \text{jets}$  production events are identified using the full SR selection criteria with the exception of the muon or electron veto. More specifically, single-muon CRs are composed of events with exactly one tight muon, and single-electron CRs are composed of events with exactly one tight electron. As described in Sec. 2, the  $p_T^{\text{miss}}$  requirement that defines the SR is replaced by an identical requirement on  $U$ , that serves as a proxy for  $p_T^{\text{miss}}$  in these CRs. To suppress the larger contribution from QCD multijet events in the single-electron CRs due to jets faking electrons, the real  $p_T^{\text{miss}}$  in each event is required to be larger than 100 GeV. An additional set of single-lepton CRs is used in this search, populated with events that meet the aforementioned single-electron or single-muon requirements, but fail the criterion on the leading AK15 jet DEEPAK15 score.

Dedicated single-lepton CRs are also used to constrain the background from  $t\bar{t}$  production. The same single-electron or single-muon selections are applied, but the veto on b-tagged AK4 jets that do not overlap with the leading AK15 jet is inverted. In this case, only CRs populated with events that satisfy the leading AK15 jet DEEPAK15 score requirement are used.

---

## 291 5 Background estimation

292 Background estimation and signal extraction are performed simultaneously, using a joint maximum  
 293 likelihood (ML) fit across all SR and CRs. A likelihood function is constructed to model  
 294 the expected background contributions in each bin of the two-dimensional U-vs- $m_{SD}$  variable  
 295 of the SR and CRs, as well as the expected signal yield in each bin of the SR. The best fit  
 296 background model, as well as the best fit signal strength modifier  $\mu$  (which—for a given sig-  
 297 nal hypothesis—controls the signal normalization relative to the theoretical cross section), are  
 298 obtained by maximizing a joint likelihood function of all SRs and CRs.

299 Separate approaches are adopted to estimate the dominant backgrounds from Z + jets, W +  
 300 jets, and t̄t productions and the subdominant backgrounds from single t, VV, H → b̄b, and QCD  
 301 multijet productions. The predictions for the dominant Z + jets, W + jets, and t̄t backgrounds  
 302 in SR are based on the yield of the same processes in each bin of the CRs. The per-bin yields  
 303 for these processes in SR are defined as free parameters of the likelihood function. The yields  
 304 in CRs are then defined relative to these parameters by introducing a set of per-bin transfer  
 305 factors. This choice of transfer factors takes into account the correlations between the Z + jets  
 306 and W + jets background contributions in all regions. In all cases, the central values of the  
 307 transfer factors are obtained from the ratios of the simulated U-vs- $m_{SD}$  spectra of the respective  
 308 processes in the SR to those in CRs. The predictions for the subdominant single t, VV, H → b̄b,  
 309 and QCD multijet backgrounds in all SR and CRs are taken directly from simulation.

310 The likelihood method relies on the accurate predictions of the ratios between the dominant  
 311 backgrounds in the SRs and CRs, as well as on the absolute normalization and shape of the  
 312 U-vs- $m_{SD}$  distributions for the subdominant backgrounds. To achieve the most accurate pos-  
 313 sible predictions for these quantities, weights are applied to each simulated event to take into  
 314 account both experimental and theoretical effects not present in the MC samples. The exper-  
 315 imental corrections are related to the trigger efficiencies, the identification and reconstruction  
 316 efficiencies of charged leptons, the efficiencies of the DEEPJET and DEEPAK15 algorithms, and  
 317 the pileup distribution in simulation. Theoretical corrections are applied to the V + jets pro-  
 318 cesses in order to model the effects of NLO terms in the perturbative EW corrections [57]. The  
 319 corrections are parameterized as a function of the generator-level boson  $p_T$  and are evaluated  
 320 separately for W + jets and Z + jets processes.

### 321 5.1 Systematic uncertainties

322 Systematic uncertainties are incorporated in the likelihood function as nuisance parameters. In  
 323 the case of the Z + jets, W + jets, and t̄t processes, the nuisance parameters affect the values  
 324 of the transfer factors in each bin of the U-vs- $m_{SD}$  variable and thus control the ratios of the  
 325 contributions from different processes, as well as the ratios of the yields in the SRs to those in  
 326 various CRs. For the subdominant background processes, the yields in each bin are directly  
 327 parameterized in terms of the nuisance parameters.

328 Uncertainties in the measurement of the integrated luminosity in each year of data taking are  
 329 0.6–2.0% [58–60]. The uncertainties in the corrections for the L1 pre-firing effect in 2016 and  
 330 2017, as well as the uncertainties in the pileup correction are of the order of 1%. The uncertain-  
 331 ties in the efficiencies of reconstructing and identifying electron candidates are 1% and 2–3%,  
 332 respectively. For muons, the uncertainties in the identification efficiency are 1%, with an ad-  
 333 dditional 1% uncertainty in the efficiency of the isolation criteria. A systematic uncertainty for  
 334 each lepton/photon veto selection has been obtained by propagating the overall uncertainties  
 335 in the identification of muons, electrons, photons, and taus, into the vetoed regions. While  
 336 the uncertainties are found to be negligible for photon, muon, and electron vetoes, a 3% un-

certainty in the tau veto is included. The uncertainties in the trigger efficiency are 1% for the single electron trigger and 1–2% for the  $p_T^{\text{miss}}$  trigger. The uncertainty in the modeling of  $p_T^{\text{miss}}$  in simulation [61] is dominated by the uncertainty in the jet energy corrections. The resulting bin migration affects the acceptance of the minimum requirement in  $p_T^{\text{miss}}$ . The resulting change in rate is estimated to be 5%, and is included as a systematic uncertainty. An additional systematic uncertainty is included to cover the effect of the uncertainties in the AK15 jet energy corrections on the AK15 jet  $p_T$ . Also in this case, the resulting bin migration affects the acceptance of the minimum requirements in AK15 jet  $p_T$ . This introduces an effect on the rate of the order of 4%. The uncertainty in the DEEPJET efficiency leads to a shape uncertainty applied to all processes in all regions. The uncertainty in the DEEPAK15 efficiency results in a shape uncertainty applied to the signal processes in SR. Uncertainties of 100% are assigned to the normalization of the QCD multijet background contributions in all of the regions. These uncertainties are correlated among the regions with the same source of fakes: one uncertainty is applied to QCD multijet events in the SR and in the CR enriched in Z + jets production events, a separate uncertainty is applied to QCD multijet events in the single-muon CRs, and another uncertainty is applied to the single-electron CRs. Additionally, uncertainties of 20% are assigned to the cross section of VV, H →  $b\bar{b}$ , and DY+jets productions. Similarly, 10% uncertainties in the single t and t $\bar{t}$  production cross sections are also assigned. The theoretical uncertainties in the transfer factors related to higher-order effects in the QCD and EW perturbative expansions are calculated according to the prescription given in Ref. [57], and implemented as described in Ref. [62]. Bin-by-bin statistical uncertainties are incorporated following the Barlow-Beeston-lite approach [63].

The likelihood functions obtained for the three data taking years are combined in order to maximize the statistical power of the search. The combination is performed by defining a combined likelihood describing all the regions in all datasets. For this purpose, the effects of all theoretical uncertainties are assumed to be correlated. Most experimental uncertainties are dominated by the inherent precision of auxiliary measurements specific to each dataset and are thus assumed to be uncorrelated among the different data taking years. The experimental uncertainties related to the determination of the integrated luminosity and to the DEEPJET efficiency are partially correlated among the data taking years, which is taken into account by splitting the total uncertainty into its correlated and uncorrelated components. A summary of all the uncertainties considered for this analysis is reported in Table 2.

Table 2: Summary of statistical and systematic uncertainties included in the analysis. The value given for each uncertainty is the maximum value.

Source	Uncertainty
Luminosity	0.6–2%
Pileup	$\mathcal{O}(1\%)$
L1 pre-firing	$\mathcal{O}(1\%)$
$p_T^{\text{miss}}$ trigger efficiency	1–2%
Single electron trigger efficiency	1%
Muon isolation efficiency	1%
Muon identification efficiency	1%
Electron reconstruction efficiency	1%
Electron identification efficiency	2–3%
$p_T^{\text{miss}}$	5%
Jet energy corrections	4%
DEEPJET efficiency	shape
DEEPAK15 efficiency	shape
VV cross section	20%
$H \rightarrow b\bar{b}$ cross section	20%
DY+jets cross section	20%
Single t cross section	10%
$t\bar{t}$ cross section	10%
QCD- $p_T^{\text{miss}}$ normalization	100%
QCD-electron normalization	100%
QCD-muon normalization	100%
Higher-order corrections	shape
Bin-by-bin statistics	shape

## 369 6 Results and interpretation

370 The ML fit is performed by combining the SR and CRs as well as the datasets corresponding  
 371 to the years of data taking. The U-vs- $m_{SD}$  distributions in SR before and after the fit (“prefit”  
 372 and “postfit”) are for all three years combined are shown in Fig. 2. Good agreement is observed  
 373 between the background-only postfit result and the data.

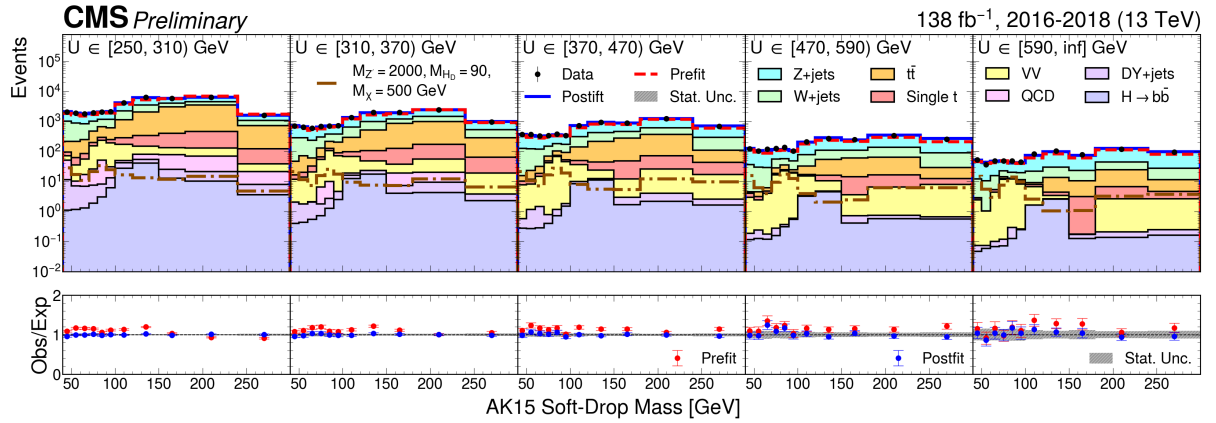


Figure 2: Postfit  $m_{SD}$  distributions in bins of  $U$  for all three years combined. Distributions in SR are shown. The top plots present stacked postfit predictions for the backgrounds superimposed on the data. The blue curve represents the postfit total background prediction, while the red curve represents the prefit one. The bottom plots present the ratio between the data (labeled as “Observed”, or “Obs”) and the background predictions (labeled as “Expected”, or “Exp”). The ratio between the data and the postfit prediction is represented by the blue dots, while the ratio between the data and the prefit prediction is represented by the red ones. Only statistical uncertainties are shown.

374 Exclusion limits on  $\mu$  are presented for different signal hypotheses. All data sets and cate-  
 375 gories are included. The exclusion limits are calculated using the  $CL_s$  criterion [64–66], and an  
 376 asymptotic approximation to the distribution of the profiled likelihood ratio test statistic.

377 Exclusion limits are calculated in the two-dimensional parameter space of the DM and media-  
 378 tor masses,  $m_{DM}$  and  $m_{Z'}$ , constrained by the fact that only scenarios in which the DM particle  
 379 is more massive than the  $H_D$  boson are considered. The coupling between the mediator and  
 380 SM quarks is set to a constant value of  $g_q = 0.25$ , and the mediator-DM coupling is set to  $g_{DM}$   
 381 = 1.0. The resulting exclusion limits at 95 % confidence level (CL) on  $\mu$  are shown in Figs. ??-  
 382 ?? for different hypotheses of the  $H_D$  boson mass. In the plots, darker shades correspond to  
 383 smaller upper limits, i.e. more stringent constraints. The solid black line represents the ob-  
 384 served 95 % CL exclusion contour, while the dashed and dotted lines indicate the median  
 385 expected exclusion and its 68 % and 95 % confidence intervals, respectively. The parameter  
 386 space inside the solid black boundary is excluded at 95 % CL under the model assumptions.  
 387 Values of the mediator mass of up to 2.5–4.5 TeV are excluded, depending on the mass of the  
 388  $H_D$  boson.

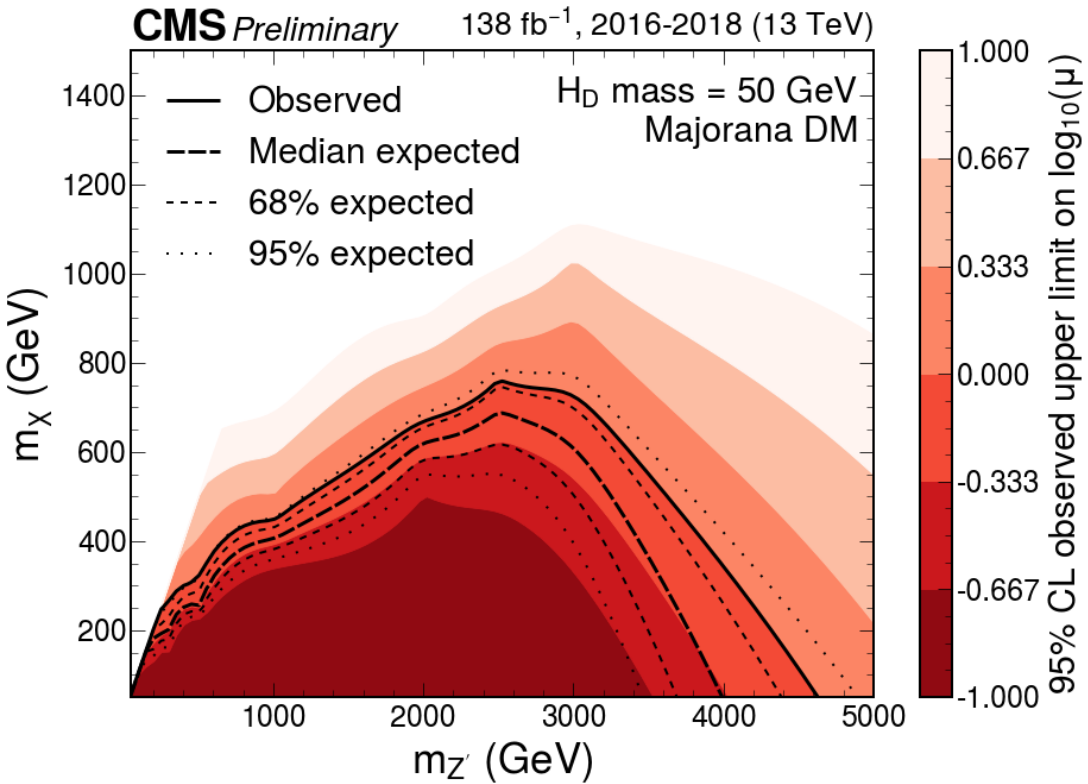


Figure 3: Expected and observed exclusion limits at 95% CL on the signal strength  $\mu = \sigma/\sigma_{\text{theo}}$  as a function of  $m_{Z'}$  for a  $H_D$  boson mass of 50 GeV. Only scenarios where the DM particle is more massive than  $H_D$  are considered. The black solid line indicates the exclusion boundary  $\mu = 1$ . Parameter combinations with larger values of  $\mu$  are excluded.

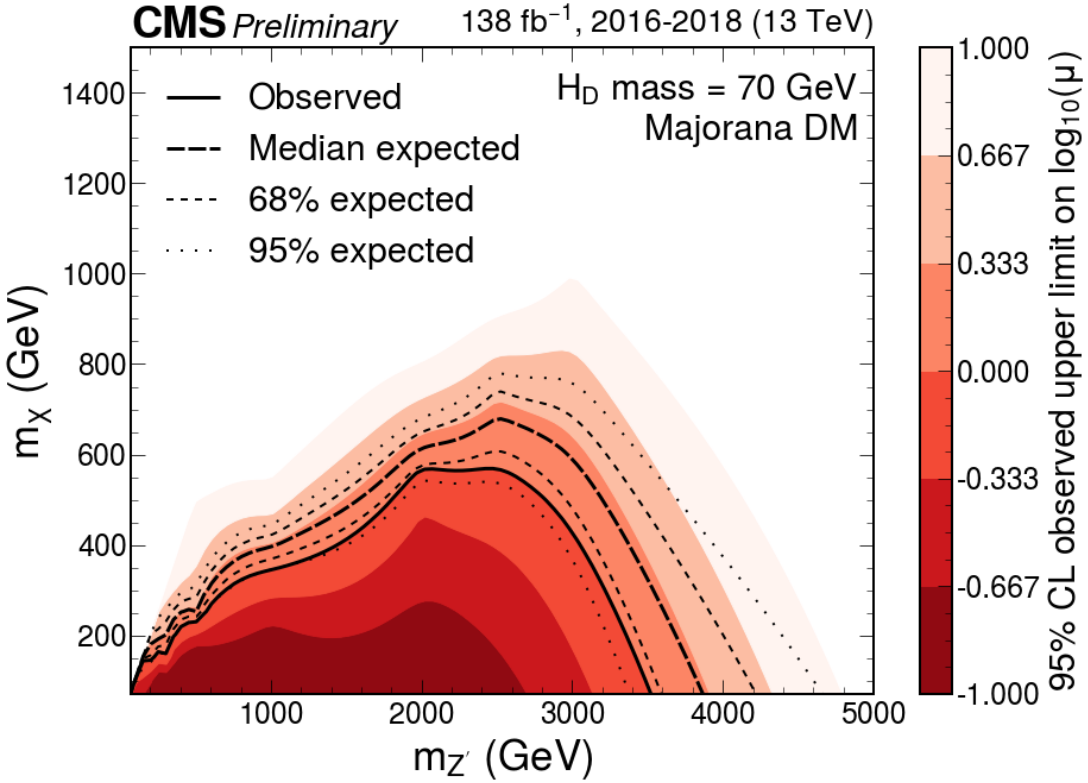


Figure 4: Expected and observed exclusion limits at 95% CL on the signal strength  $\mu = \sigma/\sigma_{\text{theo}}$  as a function of  $m_{Z'}$  for a  $H_D$  boson mass of 70 GeV. Only scenarios where the DM particle is more massive than  $H_D$  are considered. The black solid line indicates the exclusion boundary  $\mu = 1$ . Parameter combinations with larger values of  $\mu$  are excluded.

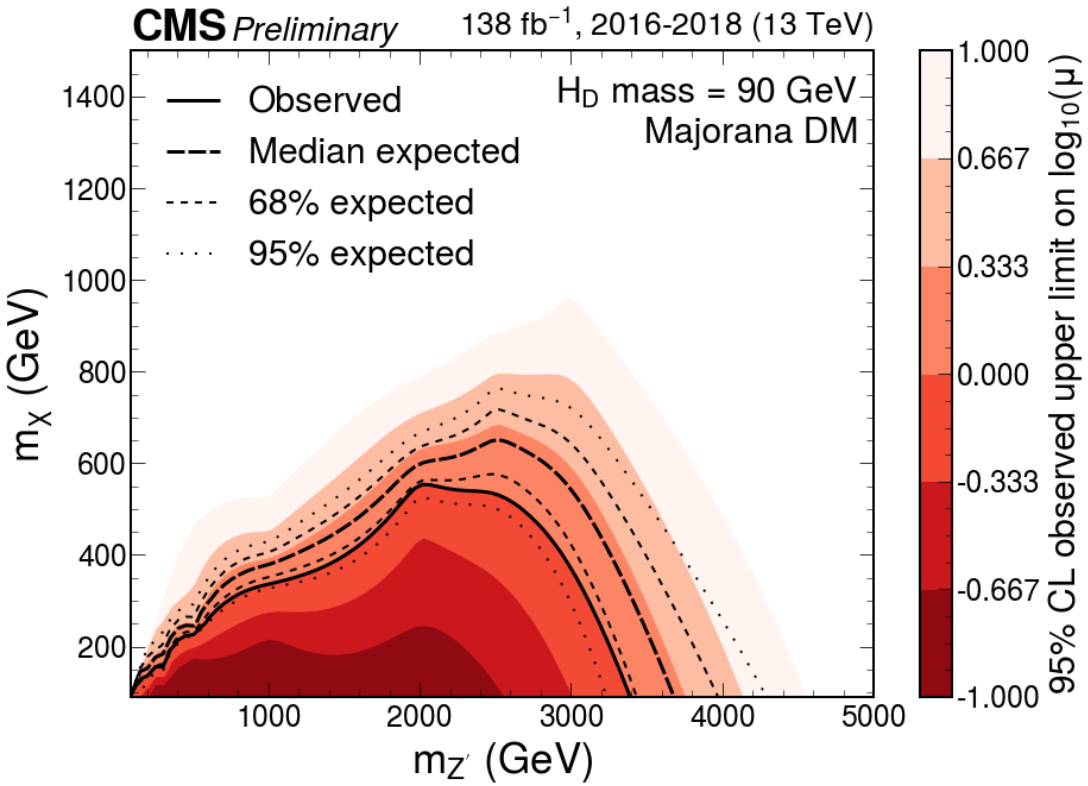


Figure 5: Expected and observed exclusion limits at 95% CL on the signal strength  $\mu = \sigma/\sigma_{\text{theo}}$  as a function of  $m_{Z'}$  for a  $H_D$  boson mass of 90 GeV. Only scenarios where the DM particle is more massive than  $H_D$  are considered. The black solid line indicates the exclusion boundary  $\mu = 1$ . Parameter combinations with larger values of  $\mu$  are excluded.

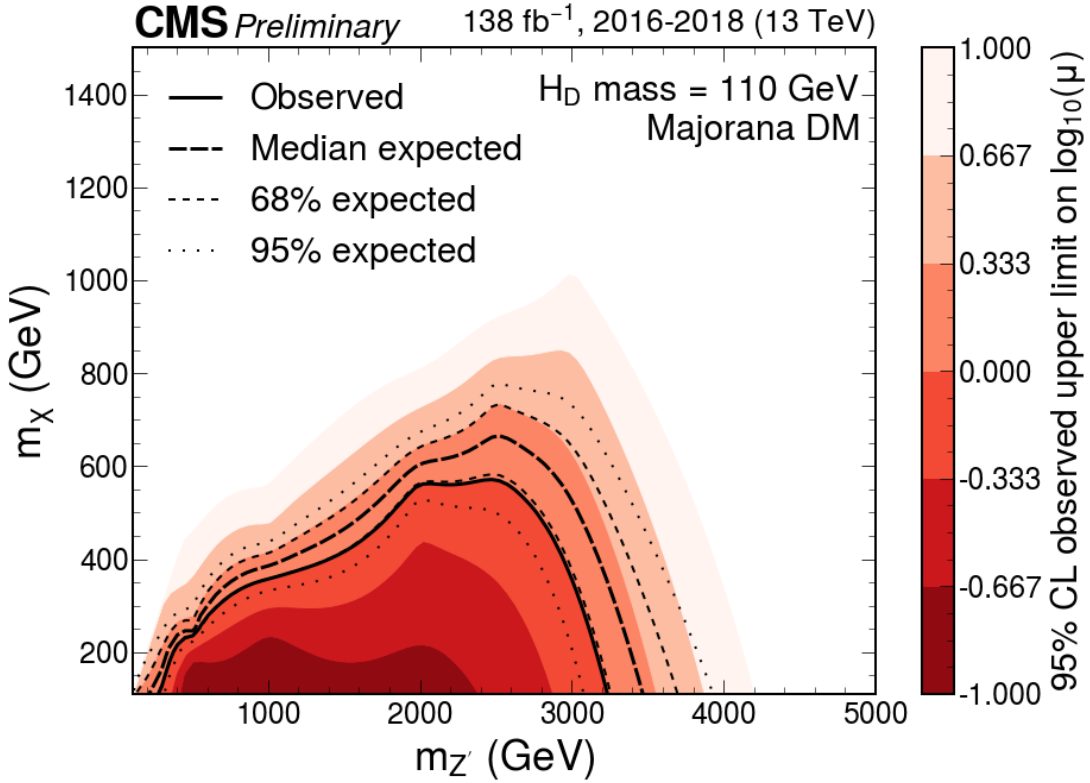


Figure 6: Expected and observed exclusion limits at 95% CL on the signal strength  $\mu = \sigma/\sigma_{\text{theo}}$  as a function of  $m_{Z'}$  for a  $H_D$  boson mass of 110 GeV. Only scenarios where the DM particle is more massive than  $H_D$  are considered. The black solid line indicates the exclusion boundary  $\mu = 1$ . Parameter combinations with larger values of  $\mu$  are excluded.

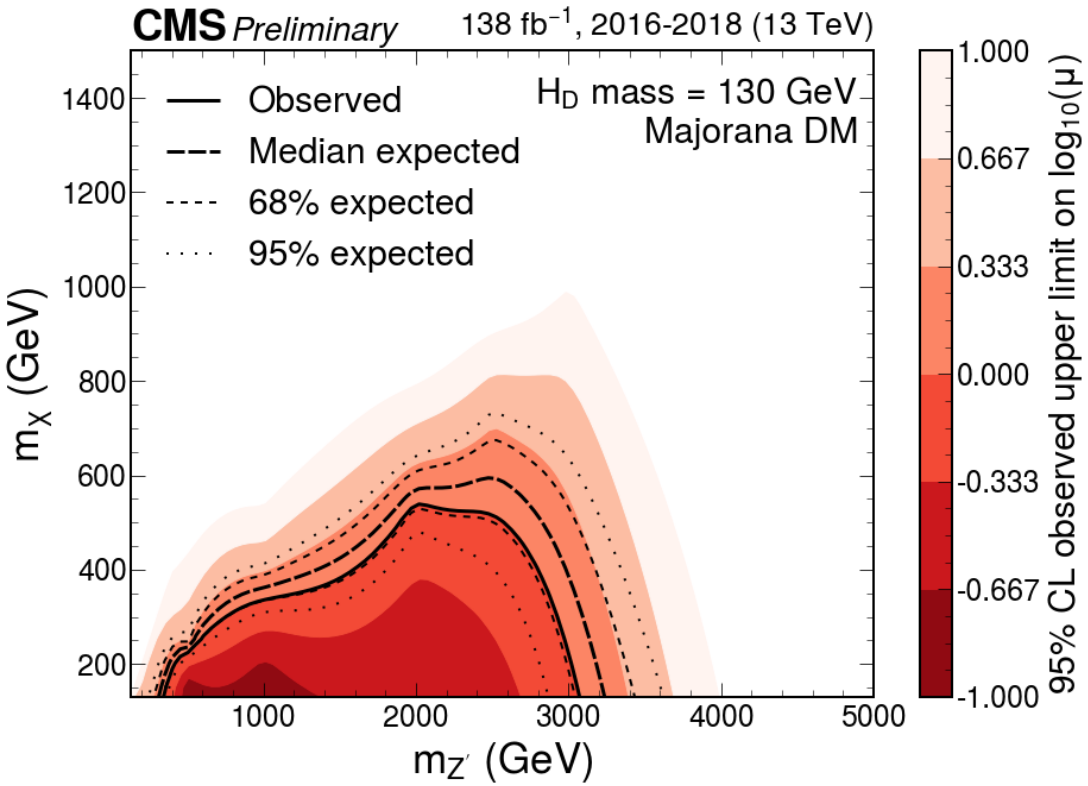


Figure 7: Expected and observed exclusion limits at 95% CL on the signal strength  $\mu = \sigma/\sigma_{\text{theo}}$  as a function of  $m_{Z'}$  for a  $H_D$  boson mass of 130 GeV. Only scenarios where the DM particle is more massive than  $H_D$  are considered. The black solid line indicates the exclusion boundary  $\mu = 1$ . Parameter combinations with larger values of  $\mu$  are excluded.

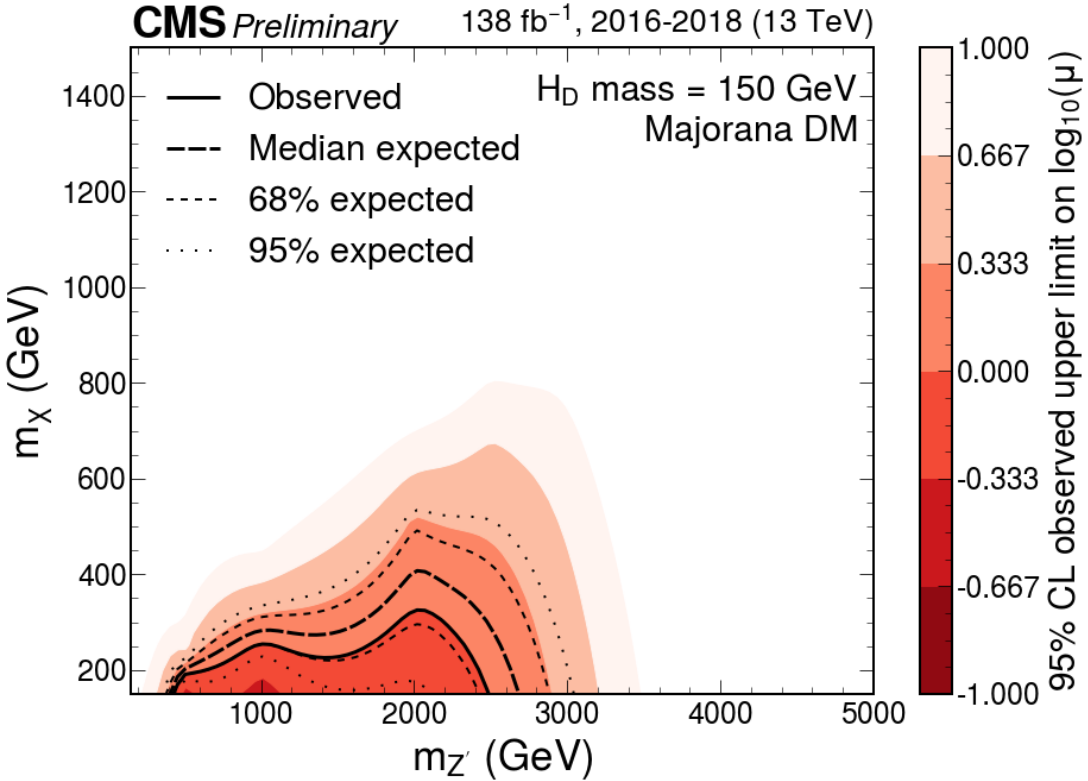


Figure 8: Expected and observed exclusion limits at 95% CL on the signal strength  $\mu = \sigma/\sigma_{\text{theo}}$  as a function of  $m_{Z'}$  for a  $H_D$  boson mass of 150 GeV. Only scenarios where the DM particle is more massive than  $H_D$  are considered. The black solid line indicates the exclusion boundary  $\mu = 1$ . Parameter combinations with larger values of  $\mu$  are excluded.

## 389 7 Summary

390 A search for physics beyond the standard model in events with a resonant b-quark pair and  
 391 large missing transverse momentum has been presented. A data set of proton-proton collisions  
 392 at a center-of-mass energy of 13 TeV, corresponding to an integrated luminosity of  $138 \text{ fb}^{-1}$  is  
 393 analyzed. A joint maximum likelihood fit over a combination of signal and control regions is  
 394 used to constrain standard model background processes and to extract a possible signal. The  
 395 result is interpreted in terms of exclusion limits at 95% confidence level on the parameters of  
 396 a model of production of a  $H_D$  boson in association with dark matter particles. Values of the  
 397 mediator mass of up to 2.5–4.5 TeV are excluded, depending on the mass of the  $H_D$  boson and  
 398 assuming the couplings of  $g_q = 0.25$  between the mediator and quarks, and  $g_\chi=1.0$  between  
 399 the mediator and the DM particles.

---

## 400 Acknowledgments

## 401 References

- 402 [1] N. Arkani-Hamed et al., “A theory of dark matter”, *Phys. Rev. D* **79** (2009) 015014,  
403 doi:10.1103/PhysRevD.79.015014.
- 404 [2] G. Bertone, D. Hooper, and J. Silk, “Particle dark matter: Evidence, candidates and  
405 constraints”, *Phys. Rept.* **405** (2005) 279–390,  
406 doi:10.1016/j.physrep.2004.08.031, arXiv:hep-ph/0404175.
- 407 [3] D. Abercrombie et al., “Dark matter benchmark models for early LHC Run-2 searches:  
408 report of the ATLAS/CMS dark matter forum”, 2015. arXiv:1507.00966.
- 409 [4] CMS Collaboration, “Search for new particles in events with energetic jets and large  
410 missing transverse momentum in proton-proton collisions at  $\sqrt{s} = 13$  TeV”, *JHEP* **11**  
411 (2021) 153, doi:10.1007/JHEP11(2021)153, arXiv:2107.13021.
- 412 [5] ATLAS Collaboration, “Search for new phenomena in events with an energetic jet and  
413 missing transverse momentum in  $pp$  collisions at  $\sqrt{s} = 13$  TeV with the ATLAS detector”,  
414 *Phys. Rev. D* **103** (2021), no. 11, 112006, doi:10.1103/PhysRevD.103.112006,  
415 arXiv:2102.10874.
- 416 [6] M. Duerr et al., “Hunting the dark Higgs”, *JHEP* **04** (2017) 143,  
417 doi:10.1007/JHEP04(2017)143, arXiv:1701.08780.
- 418 [7] N. F. Bell, Y. Cai, and R. K. Leane, “Dark Forces in the Sky: Signals from Z' and the Dark  
419 Higgs”, *JCAP* **08** (2016) 001, doi:10.1088/1475-7516/2016/08/001,  
420 arXiv:1605.09382.
- 421 [8] F. Kahlhoefer, K. Schmidt-Hoberg, T. Schwetz, and S. Vogl, “Implications of unitarity and  
422 gauge invariance for simplified dark matter models”, *JHEP* **02** (2016) 016,  
423 doi:10.1007/JHEP02(2016)016, arXiv:1510.02110.
- 424 [9] N. F. Bell, Y. Cai, and R. K. Leane, “Impact of mass generation for spin-1 mediator  
425 simplified models”, *JCAP* **01** (2017) 039, doi:10.1088/1475-7516/2017/01/039,  
426 arXiv:1610.03063.
- 427 [10] LHC Dark Matter Working Group, “Recommendations of the LHC dark matter working  
428 group: Comparing LHC searches for dark matter mediators in visible and invisible decay  
429 channels and calculations of the thermal relic density”, *Phys. Dark Univ.* **26** (2019)  
430 100377, doi:10.1016/j.dark.2019.100377, arXiv:1703.05703.
- 431 [11] M. T. Frandsen et al., “LHC and Tevatron Bounds on the Dark Matter Direct Detection  
432 Cross-Section for Vector Mediators”, *JHEP* **07** (2012) 123,  
433 doi:10.1007/JHEP07(2012)123, arXiv:1204.3839.
- 434 [12] CMS Collaboration, “A portrait of the Higgs boson by the CMS experiment ten years  
435 after the discovery.”, *Nature* **607** (2022), no. 7917, 60,  
436 doi:10.1038/s41586-022-04892-x, arXiv:2207.00043. [Erratum:  
437 doi:10.1038/s41586-023-06164-8].
- 438 [13] ATLAS Collaboration, “Search for dark matter produced in association with a dark Higgs  
439 boson decaying into  $W^+W^-$  in the one-lepton final state at  $\sqrt{s}=13$  TeV using  $139\text{ fb}^{-1}$  of

- 440        *pp* collisions recorded with the ATLAS detector”, *JHEP* **07** (2023) 116,  
441        doi:[10.1007/JHEP07\(2023\)116](https://doi.org/10.1007/JHEP07(2023)116), arXiv:[2211.07175](https://arxiv.org/abs/2211.07175).
- 442        [14] CMS Collaboration, “Search for dark matter particles in  $W^+W^-$  events with transverse  
443        momentum imbalance in proton-proton collisions at  $\sqrt{s} = 13$  TeV”, *JHEP* **03** (2024) 134,  
444        doi:[10.1007/JHEP03\(2024\)134](https://doi.org/10.1007/JHEP03(2024)134), arXiv:[2310.12229](https://arxiv.org/abs/2310.12229).
- 445        [15] ATLAS Collaboration, “Search for dark matter produced in association with a dark Higgs  
446        boson in the  $b\bar{b}$  final state using  $pp$  collisions at  $\sqrt{s} = 13$  TeV with the ATLAS detector”,  
447        arXiv:[2407.10549](https://arxiv.org/abs/2407.10549).
- 448        [16] CMS Collaboration, “The CMS experiment at the CERN LHC”, *JINST* **3** (2008) S08004,  
449        doi:[10.1088/1748-0221/3/08/S08004](https://doi.org/10.1088/1748-0221/3/08/S08004).
- 450        [17] CMS Collaboration, “Development of the CMS detector for the CERN LHC Run 3”,  
451        *JINST* **19** (2024) P05064, doi:[10.1088/1748-0221/19/05/P05064](https://doi.org/10.1088/1748-0221/19/05/P05064).
- 452        [18] CMS Collaboration, “Performance of the CMS Level-1 trigger in proton-proton collisions  
453        at  $\sqrt{s} = 13$  TeV”, *JINST* **15** (2020), no. 10, P10017,  
454        doi:[10.1088/1748-0221/15/10/P10017](https://doi.org/10.1088/1748-0221/15/10/P10017), arXiv:[2006.10165](https://arxiv.org/abs/2006.10165).
- 455        [19] CMS Collaboration, “The CMS trigger system”, *JINST* **12** (2017), no. 01, P01020,  
456        doi:[10.1088/1748-0221/12/01/P01020](https://doi.org/10.1088/1748-0221/12/01/P01020), arXiv:[1609.02366](https://arxiv.org/abs/1609.02366).
- 457        [20] CMS Collaboration, “Performance of the CMS high-level trigger during LHC Run 2”,  
458        *JINST* **19** (2024), no. 11, P11021, doi:[10.1088/1748-0221/19/11/P11021](https://doi.org/10.1088/1748-0221/19/11/P11021),  
459        arXiv:[2410.17038](https://arxiv.org/abs/2410.17038).
- 460        [21] CMS Collaboration, “Electron and photon reconstruction and identification with the  
461        CMS experiment at the CERN LHC”, *JINST* **16** (2021), no. 05, P05014,  
462        doi:[10.1088/1748-0221/16/05/P05014](https://doi.org/10.1088/1748-0221/16/05/P05014), arXiv:[2012.06888](https://arxiv.org/abs/2012.06888).
- 463        [22] CMS Collaboration, “Performance of the CMS muon detector and muon reconstruction  
464        with proton-proton collisions at  $\sqrt{s} = 13$  TeV”, *JINST* **13** (2018) P06015,  
465        doi:[10.1088/1748-0221/13/06/P06015](https://doi.org/10.1088/1748-0221/13/06/P06015), arXiv:[1804.04528](https://arxiv.org/abs/1804.04528).
- 466        [23] CMS Collaboration, “Description and performance of track and primary-vertex  
467        reconstruction with the CMS tracker”, *JINST* **9** (2014) P10009,  
468        doi:[10.1088/1748-0221/9/10/P10009](https://doi.org/10.1088/1748-0221/9/10/P10009), arXiv:[1405.6569](https://arxiv.org/abs/1405.6569).
- 469        [24] CMS Tracker Group Collaboration, “The CMS phase-1 pixel detector upgrade”, *JINST*  
470        **16** (2021) P02027, doi:[10.1088/1748-0221/16/02/P02027](https://doi.org/10.1088/1748-0221/16/02/P02027), arXiv:[2012.14304](https://arxiv.org/abs/2012.14304).
- 471        [25] CMS Collaboration, “Track impact parameter resolution for the full pseudo rapidity  
472        coverage in the 2017 dataset with the CMS phase-1 pixel detector”, CMS Detector  
473        Performance Summary CMS-DP-2020-049, 2020.
- 474        [26] CMS Collaboration, “2017 tracking performance plots”, CMS Detector Performance  
475        Summary CMS-DP-2017-015, 2017.
- 476        [27] CMS Collaboration, “Technical proposal for the Phase-II upgrade of the Compact Muon  
477        Solenoid”, CMS Technical Proposal CERN-LHCC-2015-010, CMS-TDR-15-02, 2015.
- 478        [28] CMS Collaboration, “Particle-flow reconstruction and global event description with the  
479        CMS detector”, *JINST* **12** (2017), no. 10, P10003,  
480        doi:[10.1088/1748-0221/12/10/P10003](https://doi.org/10.1088/1748-0221/12/10/P10003), arXiv:[1706.04965](https://arxiv.org/abs/1706.04965).

- [481] [29] CMS Collaboration, “Reconstruction and identification of  $\tau$  lepton decays to hadrons and  
[482]  $\nu_\tau$  at CMS”, *JINST* **11** (2016) P01019, doi:10.1088/1748-0221/11/01/P01019,  
[483] arXiv:1510.07488.
- [484] [30] C. Collaboration, “Identification of hadronic tau lepton decays using a deep neural  
[485] network”, *JINST* **17** (2022) P07023, doi:10.1088/1748-0221/17/07/P07023,  
[486] arXiv:2201.08458.
- [487] [31] M. Cacciari, G. P. Salam, and G. Soyez, “The anti- $k_T$  jet clustering algorithm”, *JHEP* **04**  
[488] (2008) 063, doi:10.1088/1126-6708/2008/04/063, arXiv:0802.1189.
- [489] [32] M. Cacciari, G. P. Salam, and G. Soyez, “FastJet user manual”, *Eur. Phys. J. C* **72** (2012)  
[490] 1896, doi:10.1140/epjc/s10052-012-1896-2, arXiv:1111.6097.
- [491] [33] CMS Collaboration, “Jet energy scale and resolution in the CMS experiment in pp  
[492] collisions at 8 TeV”, *JINST* **12** (2017) P02014,  
[493] doi:10.1088/1748-0221/12/02/P02014, arXiv:1607.03663.
- [494] [34] CMS Collaboration, “Pileup mitigation at CMS in 13 TeV data”, *JINST* **15** (2020) P09018,  
[495] doi:10.1088/1748-0221/15/09/p09018, arXiv:2003.00503.
- [496] [35] D. Bertolini, P. Harris, M. Low, and N. Tran, “Pileup per particle identification”, *JHEP* **10**  
[497] (2014) 059, doi:10.1007/JHEP10(2014)059, arXiv:1407.6013.
- [498] [36] E. Bols et al., “Jet Flavour Classification Using DeepJet”, *JINST* **15** (2020), no. 12, P12012,  
[499] doi:10.1088/1748-0221/15/12/P12012, arXiv:2008.10519.
- [500] [37] M. Dasgupta, A. Fregoso, S. Marzani, and G. P. Salam, “Towards an understanding of jet  
[501] substructure”, *JHEP* **09** (2013) 029, doi:10.1007/JHEP09(2013)029,  
[502] arXiv:1307.0007.
- [503] [38] J. M. Butterworth, A. R. Davison, M. Rubin, and G. P. Salam, “Jet substructure as a new  
[504] Higgs search channel at the LHC”, *Phys. Rev. Lett.* **100** (2008) 242001,  
[505] doi:10.1103/PhysRevLett.100.242001, arXiv:0802.2470.
- [506] [39] A. J. Larkoski, S. Marzani, G. Soyez, and J. Thaler, “Soft drop”, *JHEP* **05** (2014) 146,  
[507] doi:10.1007/JHEP05(2014)146, arXiv:1402.2657.
- [508] [40] CMS Collaboration, “Identification of heavy, energetic, hadronically decaying particles  
[509] using machine-learning techniques”, *JINST* **15** (2020), no. 06, P06005,  
[510] doi:10.1088/1748-0221/15/06/P06005, arXiv:2004.08262.
- [511] [41] CMS Collaboration, “Performance of missing transverse momentum reconstruction in  
[512] proton-proton collisions at  $\sqrt{s} = 13$  TeV using the CMS detector”, *JINST* **14** (2019)  
[513] P07004, doi:10.1088/1748-0221/14/07/P07004, arXiv:1903.06078.
- [514] [42] T. Sjöstrand et al., “An introduction to PYTHIA 8.2”, *Comput. Phys. Commun.* **191** (2015)  
[515] 159, doi:10.1016/j.cpc.2015.01.024, arXiv:1410.3012.
- [516] [43] CMS Collaboration, “Extraction and validation of a new set of CMS PYTHIA8 tunes from  
[517] underlying-event measurements”, *Eur. Phys. J. C* **80** (2020), no. 1, 4,  
[518] doi:10.1140/epjc/s10052-019-7499-4, arXiv:1903.12179.
- [519] [44] GEANT4 Collaboration, “GEANT4—a simulation toolkit”, *Nucl. Instrum. Meth. A* **506**  
[520] (2003) 250, doi:10.1016/S0168-9002(03)01368-8.

- [45] NNPDF Collaboration, “Parton distributions for the LHC run II”, *JHEP* **04** (2015) 040, doi:[10.1007/JHEP04\(2015\)040](https://doi.org/10.1007/JHEP04(2015)040), arXiv:[1410.8849](https://arxiv.org/abs/1410.8849).
- [46] NNPDF Collaboration, “Parton distributions from high-precision collider data”, *Eur. Phys. J.* **C77** (2017), no. 10, 663, doi:[10.1140/epjc/s10052-017-5199-5](https://doi.org/10.1140/epjc/s10052-017-5199-5), arXiv:[1706.00428](https://arxiv.org/abs/1706.00428).
- [47] J. Alwall et al., “The automated computation of tree-level and next-to-leading order differential cross sections, and their matching to parton shower simulations”, *JHEP* **07** (2014) 079, doi:[10.1007/JHEP07\(2014\)079](https://doi.org/10.1007/JHEP07(2014)079), arXiv:[1405.0301](https://arxiv.org/abs/1405.0301).
- [48] M. L. Mangano, M. Moretti, F. Piccinini, and M. Treccani, “Matching matrix elements and shower evolution for top-quark production in hadronic collisions”, *JHEP* **01** (2007) 013, doi:[10.1088/1126-6708/2007/01/013](https://doi.org/10.1088/1126-6708/2007/01/013), arXiv:[hep-ph/0611129](https://arxiv.org/abs/hep-ph/0611129).
- [49] R. Frederix and S. Frixione, “Merging meets matching in MC@NLO”, *JHEP* **12** (2012) 061, doi:[10.1007/JHEP12\(2012\)061](https://doi.org/10.1007/JHEP12(2012)061), arXiv:[1209.6215](https://arxiv.org/abs/1209.6215).
- [50] M. Czakon, P. Fiedler, and A. Mitov, “Total top-quark pair-production cross section at hadron colliders through  $o(\alpha_s^4)$ ”, *Phys. Rev. Lett.* **110** (2013) 252004, doi:[10.1103/PhysRevLett.110.252004](https://doi.org/10.1103/PhysRevLett.110.252004), arXiv:[1303.6254](https://arxiv.org/abs/1303.6254).
- [51] S. Alioli, P. Nason, C. Oleari, and E. Re, “NLO single-top production matched with shower in POWHEG:  $s$ - and  $t$ -channel contributions”, *JHEP* **09** (2009) 111, doi:[10.1088/1126-6708/2009/09/111](https://doi.org/10.1088/1126-6708/2009/09/111), arXiv:[0907.4076](https://arxiv.org/abs/0907.4076). [Erratum: doi:[10.1007/JHEP02\(2010\)011](https://doi.org/10.1007/JHEP02(2010)011)].
- [52] E. Re, “Single-top  $Wt$ -channel production matched with parton showers using the POWHEG method”, *Eur. Phys. J. C* **71** (2011) 1547, doi:[10.1140/epjc/s10052-011-1547-z](https://doi.org/10.1140/epjc/s10052-011-1547-z), arXiv:[1009.2450](https://arxiv.org/abs/1009.2450).
- [53] M. Aliev et al., “HATHOR: HAdronic Top and Heavy quarks crOss section calculatoR”, *Comput. Phys. Commun.* **182** (2011) 1034, doi:[10.1016/j.cpc.2010.12.040](https://doi.org/10.1016/j.cpc.2010.12.040), arXiv:[1007.1327](https://arxiv.org/abs/1007.1327).
- [54] P. Kant et al., “HATHOR for single top-quark production: Updated predictions and uncertainty estimates for single top-quark production in hadronic collisions”, *Comput. Phys. Commun.* **191** (2015) 74, doi:[10.1016/j.cpc.2015.02.001](https://doi.org/10.1016/j.cpc.2015.02.001), arXiv:[1406.4403](https://arxiv.org/abs/1406.4403).
- [55] T. Gehrmann et al., “ $W^+W^-$  production at hadron colliders in next to next to leading order QCD”, *Phys. Rev. Lett.* **113** (2014) 212001, doi:[10.1103/PhysRevLett.113.212001](https://doi.org/10.1103/PhysRevLett.113.212001), arXiv:[1408.5243](https://arxiv.org/abs/1408.5243).
- [56] J. M. Campbell and R. K. Ellis, “An update on vector boson pair production at hadron colliders”, *Phys. Rev. D* **60** (1999) 113006, doi:[10.1103/PhysRevD.60.113006](https://doi.org/10.1103/PhysRevD.60.113006), arXiv:[hep-ph/9905386](https://arxiv.org/abs/hep-ph/9905386).
- [57] J. M. Lindert et al., “Precise predictions for V+jets dark matter backgrounds”, *Eur. Phys. J. C* **77** (2017) 829, doi:[10.1140/epjc/s10052-017-5389-1](https://doi.org/10.1140/epjc/s10052-017-5389-1), arXiv:[1705.04664](https://arxiv.org/abs/1705.04664).
- [58] CMS Collaboration, “Precision luminosity measurement in proton-proton collisions at  $\sqrt{s} = 13$  TeV in 2015 and 2016 at CMS”, *Eur. Phys. J. C* **81** (2021), no. 9, 800, doi:[10.1140/epjc/s10052-021-09538-2](https://doi.org/10.1140/epjc/s10052-021-09538-2), arXiv:[2104.01927](https://arxiv.org/abs/2104.01927).

- 562 [59] CMS Collaboration, “CMS luminosity measurement for the 2017 data-taking period at  
563  $\sqrt{s} = 13$  TeV”, CMS Physics Analysis Summary CMS-PAS-LUM-17-004, 2018.
- 564 [60] CMS Collaboration, “CMS luminosity measurement for the 2018 data-taking period at  
565  $\sqrt{s} = 13$  TeV”, CMS Physics Analysis Summary CMS-PAS-LUM-18-002, 2019.
- 566 [61] CMS Collaboration, “Performance of the CMS missing transverse momentum  
567 reconstruction in pp data at  $\sqrt{s} = 8$  TeV”, *JINST* **10** (2015) P02006,  
568 doi:10.1088/1748-0221/10/02/P02006, arXiv:1411.0511.
- 569 [62] CMS Collaboration, “Search for new physics in final states with an energetic jet or a  
570 hadronically decaying W or Z boson and transverse momentum imbalance at  
571  $\sqrt{s} = 13$  TeV”, *Phys. Rev. D* **97** (2018) 092005, doi:10.1103/PhysRevD.97.092005,  
572 arXiv:1712.02345.
- 573 [63] J. S. Conway, “Incorporating Nuisance Parameters in Likelihoods for Multisource  
574 Spectra”, in *PHYSTAT 2011*, pp. 115–120. 2011. arXiv:1103.0354.  
575 doi:10.5170/CERN-2011-006.115.
- 576 [64] A. L. Read, “Presentation of search results: The  $CL_s$  technique”, *J. Phys. G* **28** (2002) 2693,  
577 doi:10.1088/0954-3899/28/10/313.
- 578 [65] T. Junk, “Confidence level computation for combining searches with small statistics”,  
579 *Nucl. Instrum. Meth. A* **434** (1999) 435, doi:10.1016/S0168-9002(99)00498-2,  
580 arXiv:hep-ex/9902006.
- 581 [66] G. Cowan, K. Cranmer, E. Gross, and O. Vitells, “Asymptotic formulae for  
582 likelihood-based tests of new physics”, *Eur. Phys. J. C* **71** (2011) 1554,  
583 doi:10.1140/epjc/s10052-011-1554-0, arXiv:1007.1727. [Erratum:  
584 doi:10.1140/epjc/s10052-013-2501-z].